Multiphoton ionization of the noble gases by an intense 10^{14}-W/cm^2 dye laser

M. D. Perry
Department of Nuclear Engineering, University of California, Berkeley, California 94720

O. L. Landen, A. Szöke, and E. M. Campbell
Lawrence Livermore National Laboratory, University of California, Livermore, California 94550

(Received 1 July 1987)

The absolute yield of multiply charged ions of the noble gases argon, krypton, and xenon as a function of laser intensity in the range of $10^{13} \leq I \leq 5\times 10^{14}$ W/cm^2 is reported. The actual numbers of ions produced using a well-characterized tunable picosecond dye laser were measured. These absolute measurements allow a direct, quantitative comparison of the data with theory. Both lowest-order perturbation theory and the "tunneling ionization" theory of Keldysh are used to model the experiment. Ionization rates obtained from the Keldysh theory are in quantitative agreement with the experimental results for production of the first charge state only. Reasons for the inability of the Keldysh theory to describe the production of multiply charged ions are discussed.

I. INTRODUCTION

The resonant and nonresonant multiphoton ionization of atoms and molecules has been extensively examined since the invention of the laser.[1-4] Nearly all of the experimental results up until about 1982 could be satisfactorily explained within the framework of lowest-order perturbation theory. Specifically, an atom with an ionization potential V_{IP} will be ionized by the absorption of N photons with energy $\hbar\omega$, where N is the first integer for which $N\hbar\omega$ exceeds the ionization potential. However, perturbation theory must eventually break down, specifically when the perturbation itself becomes comparable to or exceeds the primary interaction. The limit of lowest-order perturbation theory is very clear in laser-atom interactions, namely, when the electric field of the laser approaches that of the Coulomb field of the atom itself. In this region, one might observe previously unexpected phenomena requiring the extension of existing theories or the development of completely new theories.

One such theory is that proposed by Keldysh.[5] Keldysh derived a formula for the ionization rate of an atom in an intense field by an application of the well-known Fermi golden rule in which he used a Volkov[6] state for the outgoing electron. An important qualitative result was that the ionization rate was determined more by the properties of the outgoing electron than by the details of the atomic structure. It was also pointed out that "multiphoton ionization" and "tunneling ionization" were merely limiting cases of the general ionization of the atom by an intense electric field. Multiphoton ionization dominated in regions where the tunneling parameter γ, defined as the ratio of the field frequency ω to the tunneling frequency ω_t, was much greater than unity. On the other hand, tunneling ionization dominates for values of $\gamma \ll 1$ where

$$\gamma = \omega \frac{\sqrt{2m_e V_{IP}(0)}}{eE}, \tag{1}$$

where $V_{IP}(0)$ is the field-free ionization potential of the atom, E is the electric field strength, and e and m_e are the charge and mass of an electron.

Our work is motivated by the desire to quantitatively examine the intermediate region, $1 \leq \gamma < 4$, where perturbation theory may begin to break down. This was accomplished by measuring the ion yield of the noble gases Ar, Kr, and Xe as a function of laser intensity at $\lambda = 0.586$ μm. To our knowledge this is the first report of the observation of up to six-times-ionized xenon using a tunable picosecond dye-laser system. Furthermore, we have emphasized the detection of actual numbers of ions detected as opposed to only relative yields in an effort to facilitate direct quantitative comparison with theory. We have specifically avoided the question of intermediate high-order resonances herein, as this is the subject of a forthcoming presentation.[7]

II. EXPERIMENT

A. The laser system

The laser system used in the present experiments consists of an amplified, synchronously mode-locked dye laser. In contrast to the neodymium- or excimer-based laser systems used to date in high-order multiphoton ionization experiments, this laser is tunable. The laser begins with a cw mode-locked Nd:YAG oscillator (YAG denotes yttrium aluminum garnet) operating at 82 MHz producing 100-psec pulses at 1.064 μm (average power of 7 W). The pulse train is frequency doubled in a 5-mm potassium titanyl phosphate (KTP) crystal producing 70-psec pulses at 0.53 μm with an average power of 1.2 W. The 0.53-μm pulse train is used to synchronously

pump a linear cavity dye laser presently operated with Rhodamine 6G in enthylene glycol ($c \sim 5 \times 10^{-4} M$). The cavity length of the dye laser is tuned to match that of the Nd:YAG pump, thereby achieving mode locking in the dye laser via synchronous gain modulation. This technique provides a stable 82-MHz train of tunable radiation with each pulse having a width typically less than 5 psec and ~ 2 nJ in energy. The pulse width can be varied between 0.5 and 6 psec by cavity tuning and/or addition of small amounts of a saturable absorber to the dye jet. Frequency tuning from 0.560 to 0.630 μm is accomplished through the use of a two-plate birefringent filter placed internal to the cavity. Pulse lengths shorter than ~ 1 psec require the birefringent filter be replaced with a broader bandwidth device.

The synchronously mode-locked output of the dye laser passes through a continuously variable polarization rotator before entering the five-stage dye amplifier (Fig. 1). This allows variable control over pump and signal polarization in the amplifier. The dye amplifier itself is pumped by the second-harmonic output of a modified cavity Q-switched Nd:YAG. The Q-switched Nd:YAG operates between 1.25 and 10 Hz, providing a nearly uniform 1-cm-diameter beam. The 0.532-μm output is typically 300–350 mJ with a "three-hump" temporal distribution, the center of which is ~ 2 nsec in width. Approximately 200 mJ of the 0.532-μm output is used to pump the dye amplifier.

The dye amplifier itself consists of four dye cells separated by beam expansion telescopes and pinholes. The first two stages each have optical lengths of 2.5 cm and are transversally pumped. Pinholes between stages 1 and 2, and 2 and 3 serve both as spatial filters and to control amplified spontaneous emission (ASE). The beam expands through stage 3 and is then collimated to its final 1-cm diameter before entering the fourth stage. A saturable absorber jet of DQOCI (1,3'-diethyl 4,2'-quinolyloxadicarbo cyanineiodide) in ethylene glycol is sometimes used between stages 3 and 4 for further ASE suppression, to eliminate any prepulse and to control the leading-edge structure of the pulse (rise time). The fourth stage is double passed by the dye beam but not by the pump beam. The purpose of this last pass of the dye beam is not for further substantial amplification but rather to ensure that the beam has reached the gain-saturated regime. This substantially stabilizes pulse-to-pulse fluctuations in both energy and pulse width. Using Kiton Red 620 in methanol in the amplifier, the system provides typically 1–2-psec pulses which are continuously tunable from 0.570 to 0.600 μm. Pulse energies are typically 3 mJ with an approximately 10% ASE component spread over the range 0.580–0.583 μm. The temporal distribution of the ASE component is Gaussian with a width of 2 nsec.

The laser enters the target chamber via an optical quality vacuum window (Fig. 2) and is focused by an internal 63-mm focal length lens. The laser itself is run steady state. Intensity variation in the chamber is obtained by rotating a pair of $\lambda/10$ Glan-Thompson polarizers placed just before the vacuum window.

Initially, only the laser energy was measured on every shot. This was not sufficient to determine the focused intensity on a shot-by-shot basis owing to pulse width fluctuations. Although these fluctuations had been minimized by taking the dye amplifier to saturation, the pulse width still varied by $\sim 15\%$ from shot to shot. This led to a fluctuation in ion signal by as much as a factor of 3 for shots of the same energy. For this reason we set up an additional diagnostic to measure the peak power shot by shot in addition to the energy. This was done by utilizing the 4% reflection from the vacuum window. As shown in Fig. 2 this reflection is split, with 20% diverted to a calibrated vacuum photodiode providing an energy measurement and the remaining 80% collimated and passed through an angle tuned 250-μm-thick KDP crystal. The intensity in the crystal is kept sufficiently low so that the second-harmonic output is proportional to the square of the fundamental intensity. The harmonic output is separated from the fundamental by a series of bandpass filters and observed with another vacuum photodiode. This signal is then proportional to the time integral of $I^2(\omega)$ and hence proportional to the product of the laser power and energy. Together with the independent measurement of the energy, we obtain a measurement of the actual laser power on target on every shot. Given then that the spatial distribution at the focus does not change dramatically from shot to shot (this has been experimentally verified), an intensity measurement is obtained on a shot-by-shot basis.

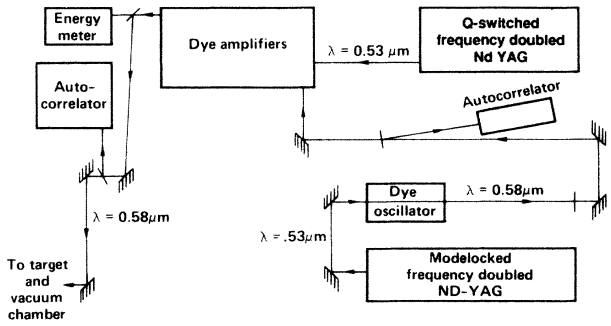

FIG. 1. Laser-system schematic.

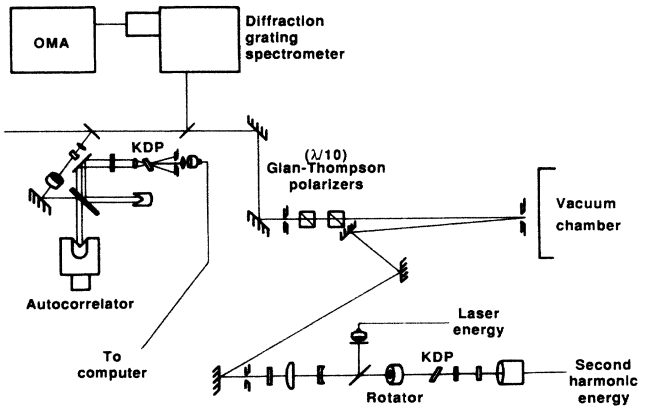

FIG. 2. Experimental optical configuration.

The laser system provides transform-limited ($\Delta\nu\Delta\tau=0.290\pm0.04$) pulses of which approximately 80% of the energy is contained in the lowest-order spatial mode. Hence, the laser pulse is very nearly Gaussian at focus [Fig. 3(b)]. The average pulse width and pulse shape is determined by multishot background-free autocorrelation.[8] The deconvolution of our autocorrelations [Fig. 3(c)] suggests a sech^2 temporal distribution which is consistent both with the theoretical pulse shape for a synchronously mode-locked dye laser and our pulse-width–bandwidth product. The intensity distribution at the focus is described by

$$I(r,z,t)=I_0F(r,z)T(t)\ , \tag{2}$$

where

$$F(r,z)=\left[\frac{1}{1+(\lambda z/\pi w_0^2)^2}\right]\exp\left[\frac{-2r^2}{w_0^2[1+(\lambda z/\pi w_0^2)^2]}\right],$$

$$T(t)=\text{sech}^2\left[\frac{2t}{\tau_p}\right],$$

$$I_0=\frac{E_{\text{pulse}}}{A\tau_p},$$

$$\tau_p=\int_{-\infty}^{\infty}T(t)dt\ ,$$

$$A=\int_0^{2\pi}\int_0^{\infty}F(r,0)r\,dr\,d\phi=\frac{\pi w_0^2}{2}\ .$$

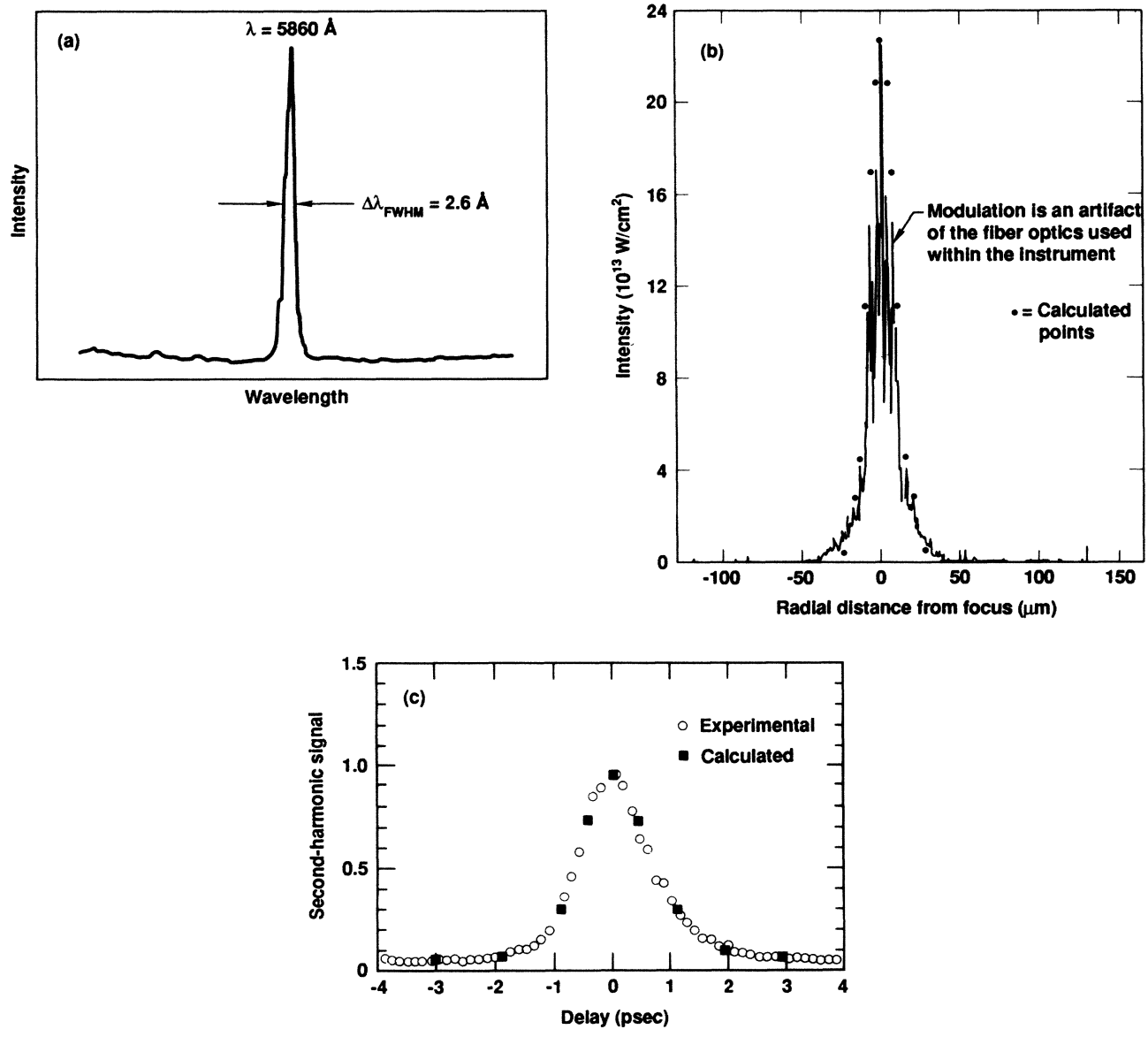

FIG. 3. Laser pulse measurements. (a) Frequency distribution, (b) horizontal lineout of spatial distribution at laser focus, calculated points are from a Gaussian fit, (c) multishot autocorrelation of amplified pulse train (repetition rate of 2.5 pulses per sec). Calculated points represent the autocorrelation of a hyperbolic-secant-squared with a full width at half maximum of 0.95 psec.

B. Experimental configuration and data acquisition

The experimental method used here in determining the ion yield as a function of laser intensity is a common one in multiphoton ionization, namely, time-of-flight ion spectrometry. However, the details of our system have some significant differences from the typical.

The system consists of a vacuum chamber pumped down to pressures less than or equal to 1×10^{-7} Torr with over 90% of the remaining background being H_2O. The target species is leaked into the chamber to a pressure of between 2×10^{-6} and 4×10^{-6} Torr via a high-precision leak valve and fills the chamber uniformly. An absolutely calibrated quadrupole mass spectrometer measures both the partial and absolute pressures of the target gas as well as that of the residual background.

The time-of-flight (TOF) ion spectrometer was designed with a resolution sufficient to completely resolve the isotopes of natural xenon. It consists of a shielded 40-cm copper drift tube connected to a pair of initially sloping then parallel metal plates which define the target region. The central 1 cm of these plates has been removed and replaced with fine metal grids. A uniform electric field of 5000 V/cm applied across these grids extracts any ion formed in the interaction region. Approximately one-third of the way down the drift tube is an electrostatic lens which allows for variation of the ion flux on the detector by regulating the dispersion of the ions in the plane perpendicular to their flight path. The ions are detected by direct impact on a 2.5-cm-diameter microchannel plate (MCP). A second microchannel plate is placed in a "chevron" configuration behind the first to boost the gain to $\sim10^6$ e^-/ion. The signal is then passed through a series of fast-timing amplifiers and on to a series of gated integrators and a digitizing oscilloscope for recording. This system has the capability to readily detect single ions.

The data recorded on every shot consists of the pulse energy, pulse power (from the second harmonic), a hardware-integrated ion signal for the singly ionized and doubly ionized species via the gated integrators, and the complete time-of-flight ion spectra as acquired by the fast transient digitizer (Tektronix 7912AD). A typical spectrum is shown in Fig. 4. Between 2000 and 3000 shots are acquired for a given species at a single wavelength. The raw data are sorted according to laser intensity and divided into approximately 200 bins. The spectra within each bin are averaged. Each peak in an averaged TOF spectrum is then integrated with the aid of a computer and the result normalized to the actual number of ions making up the signal. The result is the number of ions detected of a given charge state as a function of laser intensity.

To obtain the number of ions being produced we had to measure our absolute detection efficiency. This can be determined by utilizing the fact that once a channel in the microchannel-plate detector is struck by an ion, it cannot effectively detect any others owing to the long characteristic time (>200 μsec) for the channels to recharge. This phenomenon is easily observable for the normally Gaussian output current pulse begins to distort

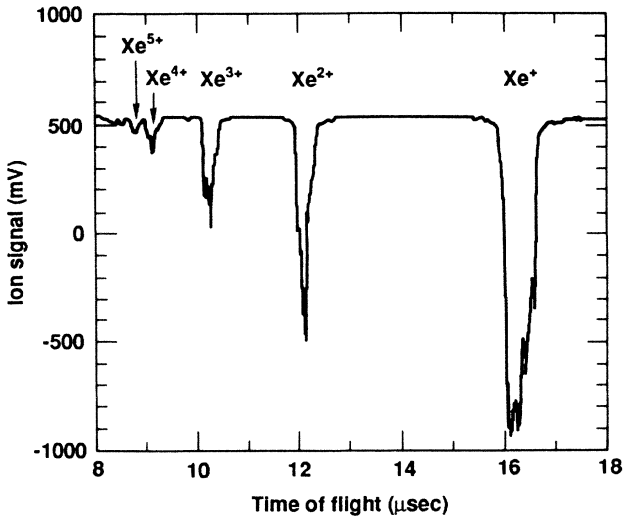

FIG. 4. Typical time-of-flight spectrum.

and eventually becomes a square pulse. This is the saturation point of the detector. By determining the area of the microchannel plate being irradiated at this saturation point, the number of channels being struck can easily be determined. The absolute detection efficiency is then just the ratio of the output signal at saturation (normalized to the number of ions) to the number of ions striking the MCP. The detection efficiency so obtained was

$$\eta_{\rm tot}=6(+4\%,-2\%)\ ,$$

which is in good agreement with the estimate of $\sim10\%$ one would obtain from the work of Fields *et al.*[9] on channeltrons.

C. Experimental results

For each of the three noble gases, Ar, Kr, and Xe, the experiment consisted of measuring the number of ions detected in a given charge state as a function of laser intensity. The experimental results are shown in Fig. 5. We note that in both argon and krypton, ions of the next higher charge state than that plotted, e.g., Ar^{4+} and Kr^{5+}, were observed.

Finally 5 actually combines the results of a series of experiments performed first with a lens system providing an approximately 10-μm ($1/e^2$ radius) focal spot and second with a lens system providing an approximately 20-μm focal spot. The reason for this lies in the fact that although the sharper focus yields a higher laser intensity, thereby allowing for the production of the higher charge states, it also results in a much smaller focal volume, resulting in a fairly small number of ions being produced below saturation. Saturation is defined here as the point at which the ionization probability for a given charge state reaches unity throughout the focal volume. This is especially true of the higher ionization states, where many more photons must be absorbed. For example, if the ionization probability below satura-

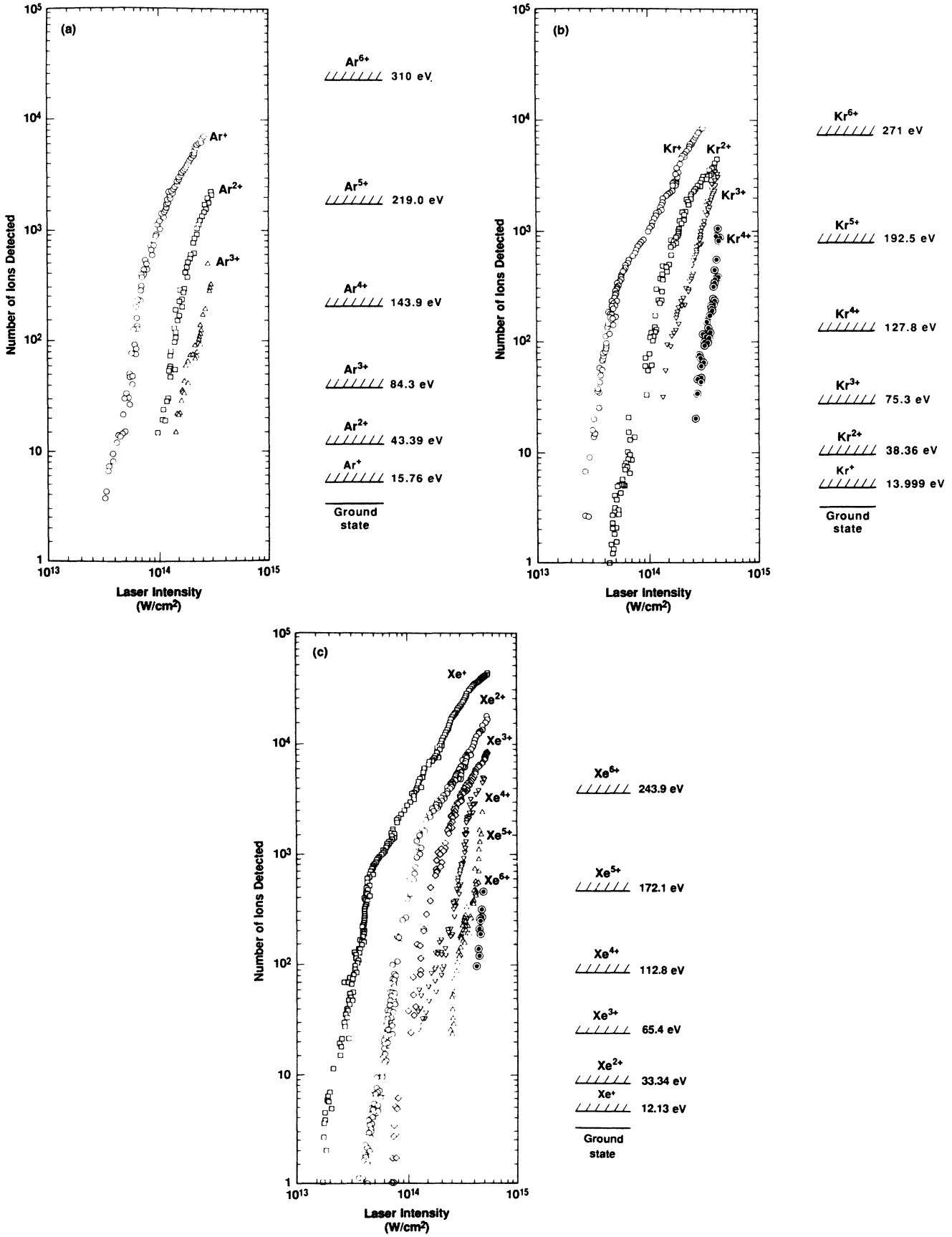

FIG. 5. Number of ions detected as a function of laser intensity. (a) Argon ($P_{ar}=1.75\times10^{-6}$ Torr), (b) krypton ($P_{Kr}=2.50\times10^{-6}$ Torr), (c) xenon ($P_{Xe}=2.67\times10^{-6}$ Torr).

tion were to follow lowest-order perturbation theory and be proportional to the Kth power of the local intensity (e.g., $Xe^{m+}+K\hbar\omega \rightarrow Xe^{(m+1)+}+e^-$), then the actual number of ions being produced below saturation would be proportional to the Kth moment of the intensity spatial distribution. For a Gaussian spatial distribution, we would have

$$\int\int\int_{-\infty}^{+\infty} F^k(x,y,z)dx\,dy\,dz = \frac{\pi^3 w_0^4}{2\lambda}\frac{(2K-5)!!}{K(2K-4)!!}\ , \quad (3)$$

where w_0 is the radius at which $I(r=w_0,z) = (1/e^2)I(0,z)$ and λ is the laser wavelength.

For a 15th-order process and $w_0=10$ μm we would have an effective focal volume of only 2.7×10^{-9} cm^3. With a target pressure of 2×10^{-5} Torr, one would be producing less than 170 ions near saturation with this number dropping rapidly below saturation. By increasing w_0 by a factor of 2, one increases the focal volume by a factor of 16, thus allowing a more extensive investigation of the region below saturation for the lower charge states while sacrificing production of the higher charge states.

Figure 5 includes data taken both at large and small f numbers. The small-f-number data were normalized to the large-f-number data simply by multiplying the number of ions detected by the ratio $(w_{01}/w_{02})^4$. This ratio can be determined empirically to quite high accuracy provided the region around saturation can be examined with both large- and small-f-number systems. This is because the number of ions produced at saturation must be in the ratio $(w_{01}/w_{02})^4$ at the same time that the saturation intensities from each measurement must be equal. The ratio of w_{01} to w_{02} determined in the present experiments was 2.11 ± 0.07. This technique allows us to examine the ion yield of the lower charge states over five orders of magnitude without having to sum over many hundreds of laser shots in regions of low ionization probability.

The fact that we extract all of the ions produced in the focus coupled with the accurate reduction of the signals to the actual number of ions detected provides us several experimental means to check for the internal consistency of our data. This also allow for direct quantitative comparison with theory and an additional method of extracting physical constants (e.g., cross sections) from the data other than relying solely on a measurement of the saturation intensity.

In Fig. 6 we give a plot of the "threshold intensity" versus the minimum number of photons absorbed. The threshold intensity is defined as the intensity at which the ionization probability is 10^{-4}. This is very nearly the intensity at which a single ion is detected per laser shot and may be obtained from Fig. 5. It should be noted that the data represent a smooth monotonically increasing curve consistent with the fact that the threshold intensity for a process requiring the nonresonant absorption of $N+1$ photons is always greater than that for a process requiring the absorption of N photons. However, the slope of this curve is also a decreasing function of photon order, which is consistent with the idea that the distinction between an $N+1$- and N-order process becomes negligible as N becomes large.

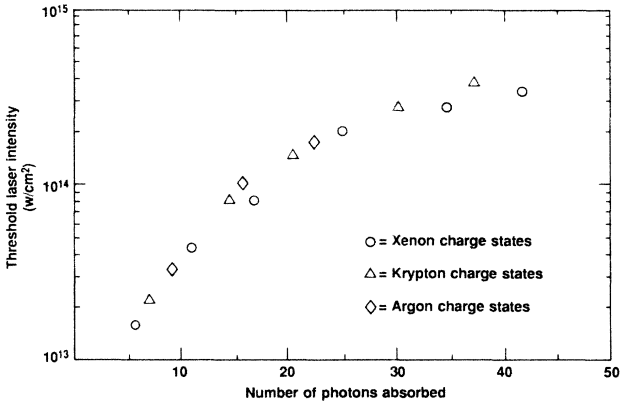

FIG. 6. "Threshold" laser intensity, defined as the intensity at which the ionization probability is 10^{-4}, as a function of the number of photons required to ionize the atom or ion to the next higher charge state.

As far as uncertainties are concerned, the uncertainty in the actual number of ions detected for a given measurement is estimated to be only about $\pm10\%$. This accuracy is attributable primarily to the fact that each experimental point plotted in Fig. 5 is actually the average of ten or more laser shots in a narrow intensity window I to $I+dI$. All of the various experimental errors are accounted for by the fluctuations in the ion yield within this bin. Thus the standard error of the measurements within a bin provides a reasonable estimate of the error for a given measurement. The average standard error over more than 100 bins is $\sim10\%$ and hence this is what we report as the standard error in ion yield for a given intensity. The uncertainty in the absolute laser intensity is more complicated. The error in the laser intensity is dominated by the uncertainty in our pulse shape and amplified spontaneous-emission fraction measurements. The laser pulse shape is measured by a deconvolution of a background-free autocorrelation taken at the beginning, middle, and end of an experimental run. Although the shape stays fairly constant, the width will drift by as much as 50% over an experimental run. Shot-to-shot pulse width fluctuations are accounted for by recording the second harmonic on each shot (see Sec. II A), however, this measurement is relative and not absolute. Hence, the systematic uncertainty in the pulse width is taken from the autocorrelations and is estimated to be $+50\%$, -20%. The uncertainty associated with the laser-energy measurement is due to the error associated with the measurement of the fraction of amplified spontaneous emission contained within the pulse. In no instance was this more than 10%. Combining the uncertainties in pulse width, ASE fraction, and spatial distribution, the uncertainty in our absolute intensity scale is estimated to be a factor of 2. Note that this is an uncertainty in the *absolute* scale, not in the relative intensity. The relative intensities are actually known to within 10% between the Ar, Kr, and Xe data.

This was accomplished simply be performing a series of large-f-number runs with mixed targets. The threshold intensities from the mixed target data provided any slight relative corrections necessary to make the three individual data sets consistent with each other.

D. Analysis and interpretation

Two models of the experiment were developed. The first is a kinetic model (rate equations) including both sequential and direct ionization with ionization rates given by lowest-order nonresonant perturbation theory. The second is also a kinetic model but with ionization rates given by the tunneling ionization theory developed by Keldysh.

In general, the evolution of the different charge states in time is given by a series of first-order coupled ordinary differential equations,

$$\frac{dn_j}{dt}=\sum_{\substack{i=0\\ i<j}} W_{ij}n_i-\sum_{k=j+1}^{Z_{\max}} W_{jk}n_j(\mathbf{r},t)\ , \tag{4}$$

where W_{ij} is the ionization rate from species i to j and $n_i(\mathbf{r},t)$ is the number density of species i at a specific point in space, $\mathbf{r}$ at a time, t. $Z_{\max}$ is the maximum charge state. One then substitutes expressions for the ionization rate and attempts a solution to the previous series. The number of ions produced is obtained by integrating the solution for the number density over the intensity spatial distribution.

E. Perturbation theory

Lowest-order perturbation theory yields a simple relationship between the ionization rate W_{ij} and the laser intensity $I(\mathbf{r},\omega,t)$,

$$W_{ij}=\sigma_{ij}^{(K)}(\omega)I^K(\mathbf{r},\omega,t)\ , \tag{5}$$

where K is the minimum number of photons by which the process $i\rightarrow j$ may proceed, ω is the laser frequency, and $\sigma_{ij}^{(K)}(\omega)$ is the Kth-order frequency-dependent cross section.

Before proceeding to solve the system, we took advantage of an important simplification dictated by the data. Note from Fig. 6 that the threshold intensity for the formation of the n_{i+3} species is sufficiently higher than that for the formation of the n_{i+2} species that direct transitions of the form $W_{i\rightarrow i+3}$ will be negligible relative to direct transitions $W_{i+1\rightarrow i+3}$. Hence the system simplifies to the following for $i=0,1,\ldots,j$:

$$\frac{dn_0}{dt}=-(\sigma_{01}^{(K_{01})}I^{K_{01}}+\sigma_{02}^{(K_{02})}I^{K_{02}})n_0\ ,$$

$$\frac{dn_1}{dt}=\sigma_{01}^{(K_{01})}I^{K_{01}}n_0-(\sigma_{12}^{(K_{12})}I^{K_{12}}+\sigma_{13}^{(K_{13})}I^{K_{13}})\ ,$$

$$\times n_1(\mathbf{r},t)\ , \tag{6}$$

$$\frac{dn_j}{dt}=\sum_{i=j-2}^{j-1}\sigma_{ij}^{(K_{ij})}I^{K_{ij}}n_i-\sum_{i=j+1}^{j+2}\sigma_{ij}^{(K_{ij})}I^{K_{ij}}n_j(r,t)\ .$$

This system was solved by a Runge-Kutta method for charge states up to Xe^{6+}, Kr^{5+}, and Ar^{4+}, respectively. The conservation condition that the total species density at any point must equal the initial target density,

$$n_0(\mathbf{r},-\infty)=\sum_{i=1}^{6} n_i(\mathbf{r},t)\ , \tag{7}$$

was used to check the calculation. Before discussing the results of this calculation, first consider the analytic solution for the total number of ions produced.

Assume that the ionization is purely sequential. This reduces the equation for n_0 to (with $K_{01}\rightarrow K_1$)

$$\frac{dn_0}{dt}=-\sigma_{01}^{(K_1)}I^{K_1}n_0\ .$$

With the intensity distribution separable, $I(r,t)=I_0F(r)T(t)$, and the initial condition that all of the target atoms are initially in their ground state, the density of neutrals is given by

$$n_0(r,t)=n_0(\mathbf{r},-\infty)\times\exp\left[-\sigma^{(K_1)}I_0^{K_1}F^{K_1}(\mathbf{r})\int_{-\infty}^{t}T^{K_1}(t)dt\right]\ . \tag{8}$$

The number of neutrals remaining in the interaction region at any time t is then determined by integrating over volume. Taking the limit as $t\rightarrow\infty$ and noting that the total number of ions produced is simply the difference in the number of neutrals in the interaction region before and after the laser pulse,

$$N_{\text{ions}}=\int\int\int_{-\infty}^{\infty} n_0(\mathbf{r},-\infty)\left[1-\exp\left[-\sigma^{(K_1)}I_{01}^{K_1}F^{K_1}(\mathbf{r})\int_{-\infty}^{\infty}T^{K_1}(t)dt\right]\right]dx\,dy\,dz\ . \tag{9}$$

For a hyperbolic-secant-squared temporal distribution, the time integral is easily performed, yielding

$$\tau_p^{(K)}=\int_{-\infty}^{\infty}T^K(t)dt=2^{K-1}\frac{(K-1)!}{(2K-1)!!}\tau_p\ , \tag{10}$$

where

$$\tau_p=\int_{-\infty}^{\infty}T(t)dt\ .$$

Although this result is quantitatively applicable to only our pulse shape, the quantitative result is quite general and shows that below saturation, the higher-order processes are increasingly dominated by only the peak of the intensity distribution. For example, below saturation, Xe^+ ($K=6$) will be produced primarily in a time which is only 37% of the total, while Kr^+ ($K=7$) will be produced primarily in a time encompassing only 34%

of τ_p, etc.

Defining a saturation intensity I_{sat} as the intensity at which the argument of the exponential at the spatial peak of the pulse reaches unity, i.e.,

$$\sigma^{(k)} I_{\text{sat}}^{K} \tau_p^{(K)} = 1 , \tag{11}$$

Eq. (9) may be rewritten as

$$N_{\text{ions}} = \int_{-\infty}^{\infty} n_0(\mathbf{r}, -\infty) \times \left\{ 1 - \exp\left[- \left[\frac{I_0 F(\mathbf{r})}{I_{\text{sat}}} \right]^{K_1} \right] \right\} dx\, dy\, dz . \tag{12}$$

With the spatial distribution $F(\mathbf{r})$ known, Eq. (9) or Eq. (12) provides a direct comparison of the experimental results with theory. The only adjustable parameter is the cross section $\sigma^{(K)}$ or, equivalently, the saturation intensity I_{sat}. This result also shows that the Kth-order dependence of the ion yield on intensity is valid only well below saturation, where a first-order expansion of the exponential yields

$$N_{\text{ions}} = \left[\frac{I_0}{I_{\text{sat}}} \right]^{K} \int\int\int_{-\infty}^{\infty} n_0(\mathbf{r}, -\infty) F^K(\mathbf{r}) dx\, dy\, dz . \tag{13}$$

Equation (3) gives the spatial integral over a Gaussian distribution. Again the result is quantitatively applicable only to Gaussian pulses, but illustrates the general qualitative result that the volume over which ions are produced is a strong function of the order of the process K. One can use this general result to calculate the number of ions formed beyond saturation. It is well known that the formation of ions above the saturation intensity is due to the expanding focal volume (i.e., the "spatial wings").[10] To a good approximation the number of ions formed above the saturation intensity will be equal to the number of atoms contained within the volume for which the laser intensity is greater than I_{sat}. For a Gaussian pulse, this volume can be determined analytically with the result

$$V\left[\frac{I_0}{I_{\text{sat}}} \right] = \frac{\pi^2 w_0^4}{\lambda} \left(\tfrac{2}{9} Z_m^3 + \tfrac{4}{3} Z_m - \tfrac{4}{3} \tan^{-1} Z_m \right) , \tag{14}$$

where $Z_m = \sqrt{I_0/I_{\text{sat}} - 1}$. For $I_0 \gg I_{\text{sat}}$ this shows that the interaction volume and, hence, the number of ions produced will be proportional to $I_0^{3/2}$. Again this is a general result independent of the specific spatial distribution. (A different result is generally obtained when focusing with other than spherical lenses, e.g., a cylindrical focus yields an eventual I_0^2 dependence.)

F. Inclusion of the "ponderomotive" potential

The photoelectron resulting from multiphoton ionization is not born in a field-free region. Rather, the outgoing electron experiences an intense, oscillating electromagnetic field. The energy required to place an electron in such a field is simply the quiver or "ponderomotive"[11] energy and is given by

$$U_p(I) = \frac{1}{4} \left[\frac{e^2 A^2}{m_e c^2} \right] = 9.33 \times 10^{-14} I \lambda^2 \text{ eV} , \tag{15}$$

where I is the local field intensity in W/cm^2 and λ is the wavelength of laser light in microns. This energy acts as an additional barrier which must be overcome by the outgoing photoelectron or, equivalently, as an increase in the ionization potential. Specifically, as discussed by Mittelman,[12] the ionization potential of the atom within the field is given by

$$V_{\text{IP}}(I) = V_{\text{IP}}(0) + U_{pe}(I) + U_p(I)_{\text{ion}} + \Delta E_{a\ \text{Stark}} - \Delta E_{i\ \text{Stark}} , \tag{16}$$

where $\Delta E_{a\ \text{Stark}}$ and $\Delta E_{i\ \text{Stark}}$ are the ground-state ac Stark shifts of the atom and ion, and U_{pe} and U_{pi} are the ponderomotive energies of the electron and residual ion, respectively. In the case of the noble gases irradiated by lasers operating in the near uv and visible regions of the spectrum the ac Stark shifts of the atomic and ionic ground states are usually negligible relative to the ponderomotive energy of the outgoing electron. Furthermore, from the inverse dependence on the mass, the quiver energy of the residual ion will always be negligible relative to that of the electron. Since there is a spatial and temporal distribution of laser intensity at the focus, there is also a spatial and temporal distribution of the ponderomotive potential. The ionization potential of the atoms contained within the interaction volume is then a function of position and time.

For the intensities considered here, the ponderomotive potential may be as high as several electron volts and is, therefore, not negligible. This is sufficient to require the absorption of an additional photon in order to overcome the ponderomotive barrier. This elimination of the lowest-order channel has been experimentally demonstrated, first by Kruit *et al.*[13] and later by Bucksbaum.[14]

It is not *a priori* obvious how to account for the ponderomotive barrier within the context of perturbation theory. One might expect that since the ionization must proceed by the absorption of additional photons, the dependence of the ion yield on intensity would change from I^K to I^{K+S}, where S is the number of additional photons absorbed. However, the intensity dependence of the yield of ions produced by these above-threshold processes has been measured[13] and found to be equal to the threshold dependence. This suggests instead that when the barrier is sufficient to close the lowest-order channel, the ionization proceeds via a two-step mechanism. The first step is the promotion of the electron to the continuum with the electron remaining bound to the vicinity of the nucleus by the ponderomotive barrier. In the second step, the system is then ionized by the absorption of additional photons. The first step is taken to be rate limiting and therefore determines the nonlinear order. This

is the model proposed by Kruit and will be adopted here.

The results of the calculations with the single adjustable parameter I_{sat} for each species are shown in Fig. 7. The solid curves represent the "best fit" to the data. Note that in the case of both kyrpton and xenon there is a general depression in the experimental ion yield above saturation from that expected. This discrepancy is not large. Furthermore, the general shape of the increase in the ion yield above saturation is near that predicted and eventually approaches $I_0^{3/2}$.

One explanation for the depression in the ion yield above saturation is simply the fact that our spatial distribution is not exactly Gaussian but only nearly so. This may also account for the deviations from a smooth nonlinear dependence on intensity of the ion yield of some of the higher charge states. For example, the strong nonlinear dependence of the ion yield of Xe^{5+} on intensity below $I_0=3.5\times10^{14}$ W/cm^2 could be dominated by ion production from a central spatial mode. Xe^{5+} production from this mode could conceivably saturate at approximately 3.6×10^{14} W/cm^2. At the point, measured as $I_0=4\times10^{14}$ W/cm^2, the Xe^{5+} signal again exhibits a strong nonlinear dependence upon intensity which may, in fact, be simply the manifestation of an additional spatial mode beginning to contribute to Xe^{5+} production. The fact that we do not observe significant spatial modulation of the focal intensity distribution does not necessarily rule this out. Even a small spatial modulation ($\sim10\%$) could lead to inflection in the Xe^{5+} yield owing to the high nonlinear order of the process. Our measurements of the spatial distribution did not have the sensitivity to observe structure at this detail. Such structure would not be evident in the ion yield of the lower charge states since there, the lower order of nonlinearity, would require a substantially larger spatial modulation in order to be observed as an inflection in the ion yield.

Other explanations for the inflection in the ion yield exist, two of which seem plausible. The first of these in-

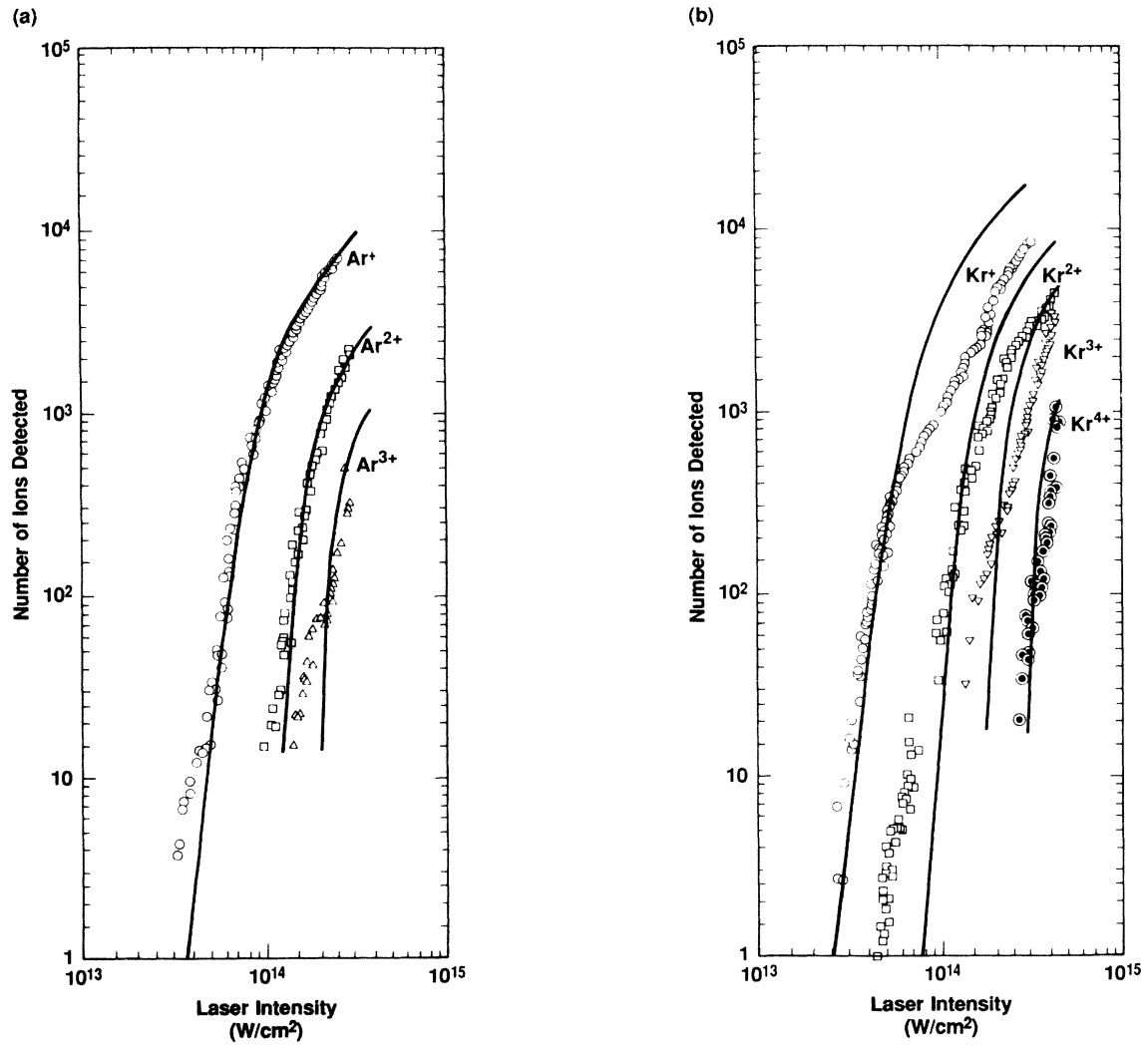

FIG. 7. Results of model calculation fits to the data using perturbation-theory ionization rates. The best-fit cross sections corresponding to the solid curves are given in Table I. (a) argon (b) krypton, and (c) xenon.

volves the ponderomotive energy discussed earlier, while the second involves the contribution of "direct processes" to the ion yield.

Consider a realistic laser pulse incident on an isolated atom or ion. The laser intensity experienced by the atom increases with time on the leading edge of the pulse. As the laser intensity is raised, so too is the ponderomotive barrier. If the Nth-order ionization rate is too low to result in the ionization of a significant fraction of the target species before the ponderomotive barrier has increased to the point at which ionization through the lowest-order channel is cutoff, then there would be a suppression in the ion yield. This suppression is due to the fact that the atom must now absorb an additional photon in order for the electron to overcome the ponderomotive barrier This suppression will last over only a small intensity range as the $N+1$th-order ionization rate will quickly equal the Nth-order rate. The Keldysh treatment accounts for this phenomenon explicitly and will be discussed in greater detail in Sec. II G. In the practical case where there is a spatial distribution as well as temporal distribution of intensity, such a suppression in the ion yield could not be observed. The phenomenon would instead be manifest as an inflection in the ion-yield curve with the magnitude of the inflection increasing with charge state. The dependence on charge state is a result of the fact that an increase in nonlinear order results in a decrease of the effective focal volume and therefore an increased sensitivity to discontinuities in the ionization rate. In the limit of a uniform spatial intensity distribution, any discontinuity in the ionization rate as a function of intensity would be mapped directly to a corresponding discontinuity in ion yield. This explanation is not only qualitatively supported by the appearance of the data but is also somewhat quantitative, owing to the fact that the inflections occur near the points where an additional photon is required to overcome the barrier.

Another plausible explanation for the inflections in ion yield is due to the contribution of direct processes to the formation of the higher charge states.[15] As mentioned previously, these direct processes are included in the rate-equation model. Slightly better fits to the data relative to those assuming purely sequential ionization can be obtained. However, our belief is that this is a purely numerical result owing to the fact that one is now al-

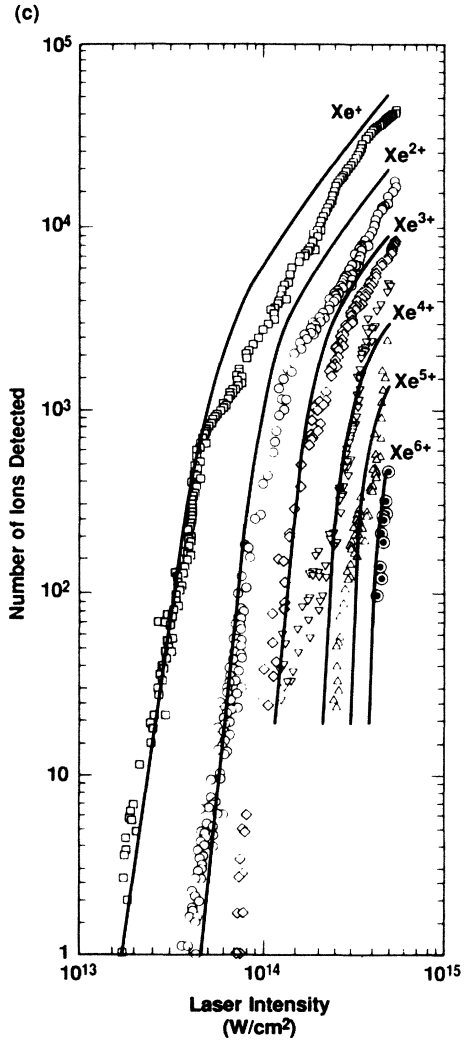

FIG. 7. (*Continued*).

lowed two parameters to fit each curve rather than one. Furthermore, the cross sections obtained for the simultaneous removal of two electrons were so large relative to those obtained for the removal of a single electron that no physical meaning could be attached to the results. The contribution of direct processes can be further investigated by plotting the threshold intensity defined earlier as a function of the number of photons absorbed. When direct processes are included, there is no clear dependence of threshold intensity on nonlinear order. On the other hand, if the data are interpreted as that resulting from purely sequential ionization, a smooth, monotonic increase in threshold intensity as a function of photon order is observed (Fig. 6). Thus we conclude that *the production of higher charge states in our experiments proceeds via a mechanism of sequential ionization.*

The determination that the ionization follows a sequential mechanism is an important one and results in substantial simplification of the rate equations. The saturation intensities and associated cross sections resulting from an overall best fit to the data including all charge states are given in Table I.

G. Keldysh theory

Returning again to Fig. 6, note that the threshold intensities for nonresonant multiphoton ionization seem to be determined primarily by the order of the process and not by the details of the atomic or ionic system. The photon order is of course determined by the atom via the ionization potential but this is a gross feature of the atomic system. There is a slight increase in the threshold curve as we proceed from xenon to argon. However, this seems to be a secondary effect. In other words, to first order, it appears that any atomic or ionic system with the same ionization potential will exhibit similar threshold intensities for nonresonant multiphoton ionization. This in turn suggests that the physics of the process is dominated instead by the outgoing electron.

Keldysh arrived at this same conclusion by a straightforward application of Fermi's golden rule. The advance made by Keldysh was the use of a properly "dressed" wave function for the outgoing electron, i.e., a Volkov state. His result for the ionization rate is

$$W = A\omega \left[\frac{V_{\mathrm{IP}}(0)}{\hbar\omega}\right]^{3/2} \left[\frac{\gamma}{\sqrt{1+\gamma^2}}\right]^{5/2} S\left[\gamma, \frac{V_{\mathrm{IP}}(\omega)}{\hbar\omega}\right] \times \exp\left[-\frac{2V_{\mathrm{IP}}(\omega)}{\hbar\omega}\left[\sinh^{-1}\gamma - \gamma\frac{(1+\gamma^2)^{1/2}}{1+2\gamma^2}\right]\right], \tag{17}$$

where $V_{\mathrm{IP}}(0)$ is the field-free ionization potential,

$$V_{\mathrm{IP}}(\omega) = V_{\mathrm{IP}}(0) + \frac{e^2E^2}{4m_e\omega^2},$$

$$S\left[\gamma, \frac{V_{\mathrm{IP}}(\omega)}{\hbar\omega}\right] = \sum_{m=0}^{\infty} \left\{\exp\left[-\left[2\left\langle\frac{V_{\mathrm{IP}}(\omega)}{\hbar\omega}+1\right\rangle - \frac{V_{\mathrm{IP}}(\omega)}{\hbar\omega}+m\right]\left[\sinh^{-1}\gamma - \frac{\gamma}{(1+\gamma^2)^{1/2}}\right]\right]\right\} \times \Phi\left\{\left[\frac{2\gamma}{(1+\gamma^2)^{1/2}}\left[\left\langle\frac{V_{\mathrm{IP}}(\omega)}{\hbar\omega}+1\right\rangle - \frac{V_{\mathrm{IP}}(\omega)}{\hbar\omega}+m\right]\right]^{1/2}\right\},$$

$$\Phi(x) = \int_0^x e^{t^2-x^2}dt,$$

$\langle (V_{\mathrm{IP}}(\omega)/\hbar\omega)+1\rangle$ is the minimum number of photons required to ionize, γ is the tunneling parameter defined in Eq. (1), and A is a numerical factor of order unity to account for a weak dependence upon the details of the atom.

Equation (17) is the full Keldysh formula and may therefore appear different to the more common limiting forms cited in the literature. The complete result should be applicable at any value of the tunneling parameter γ and not just in the tunneling regime $\gamma \ll 1$ of the multiphoton regime $\gamma \gg 1$. We are in fact required to use the complete expression as our experiments cover the range $1 \leq \gamma \leq 4$ and can therefore be considered to lie in an intermediate regime.

We have used the Keldysh result as an alternative expression for the ionization rate in our kinetic model discussed previously. Note, however, the important difference between the Keldysh and perturbation-theory expressions for the ionization rate. Keldysh's expression provides for the direct calculation of ionization rates with only minor variations in the constant A. In conventional perturbation theory this is possible only in principle. The results of our calculations along with the data are shown in Fig. 8. Note that in all cases the predicted ion yield has a slightly lowest-order dependence on intensity than I^N.

The results of our calculations show a fair quantitative agreement with the experimental results for the total

TABLE I. Fitting parameters for perturbation-theory kinetic model (sequential ionization).

	Saturation intensity ($\times 10^{14}$ W/cm^2) I_{sat}	Photons required to ionize species $(j-1)$ (neglecting ponderomotive potential)	Nth-order cross section $\sigma^{(N)}$ ($W^{-N}cm^{2N}sec^{-1}$)	Ratio of number of ions in charge state j to that in charge state $(j+1)$ at I_{sat}
Ar^+	0.67±0.03	8	5×10^{-99}	1000
Ar^{+2}	1.42±0.06	14	2×10^{-186}	>40
Ar^{+3}	2.2 ±0.1	20	5×10^{-275}	
Kr^+	0.54±0.04	7	1.5×10^{-84}	2600
Kr^{+2}	1.2 ±0.1	12	3×10^{-157}	>1000
Kr^{+3}	1.9 ±0.2	18	3×10^{-245}	
Kr^{+4}	3.1 ±0.2	25	2×10^{-350}	
Xe^+	0.42±0.03	6	3×10^{-70}	370
Xe^{+2}	0.80±0.06	11	3×10^{-141}	180
Xe^{+3}	1.42±0.06	16	1×10^{-214}	~20
Xe^{+4}	2.4 ±0.1	23	6×10^{-319}	>100
Xe^{+5}	3.3 ±0.2	29	4×10^{-409}	>50
Xe^{+6}	4.2 ±0.3	34	3×10^{-485}	

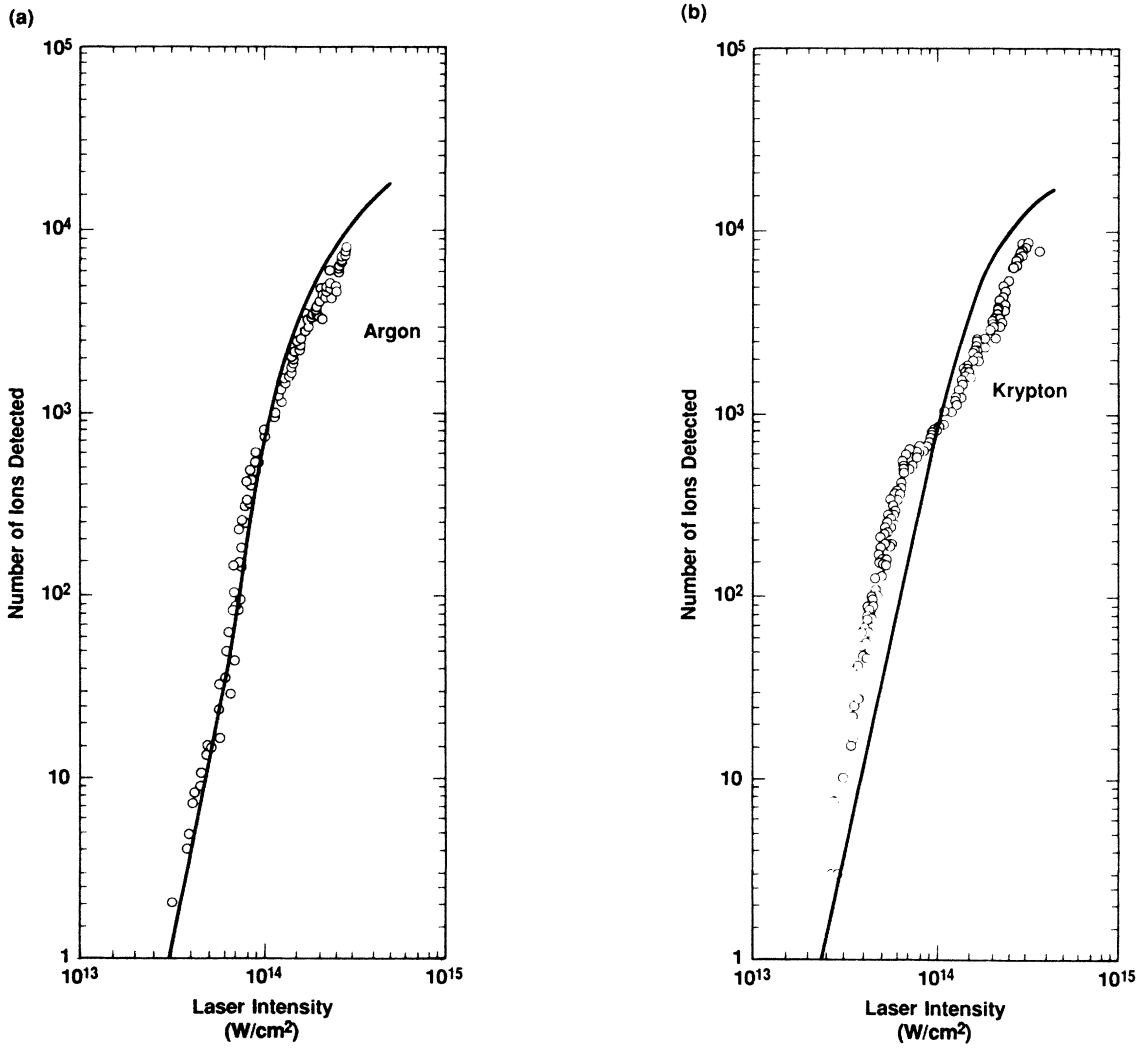

FIG. 8. Total numbers of ions detected as a function of laser intensity. The solid curve is the result of our Keldysh-theory calculations using Eq. (17): (a) argon, $A=24$; (b) krypton, $A=18$; (c) xenon, $A=4$.

number of ions produced (which is dominated by the first charge state) with values of A of order unity. Furthermore, we find a remarkable agreement between the calculated and empirical threshold intensities for the first charge state. The generally lower ion yield above saturation in the case of Kr and Xe than that predicted by the calculation is quantitatively similar to the discrepancy with the perturbation-theory-model calculations. Again this may be due simply to the fact that our focal distribution is not Gaussian but only nearly so.

The Keldysh-model calculations break down rapidly when applied to the higher charge states in that we are forced to use nonrealistically large values of the constant A ($A > 10^4$) in order to obtain a fit to the data. This is not all that surprising since Keldysh failed to account for the Coulomb field of the ion on the outgoing electron. He somewhat arbitrarily introduces the factor

$$A\left[\frac{V_{\mathrm{IP}}(0)}{\hbar\omega}\right]\frac{\gamma}{(1+\gamma^2)^{1/2}}$$

to correct for this. However, this factor is clearly inadequate when the formula is used to calculate the ionization rate of ions. This is due to the fact that the distortion of the free-electron wave function in the presence of a strong Coulomb field can be quite significant. Furthermore, the density of final states is also modified significantly by the Coulomb field from that used by Keldysh. The use of a simple WKB-type wave function modified by the presence of the laser field shows qualitatively that the presence of the Coulomb field will actually increase the ionization rate over that predicted by Keldysh. This is due primarily to the fact that the magnitude of the electrons' momentum is not $|p_{\mathrm{free}}|$ but rather

$$|p| \sim (p_{\mathrm{free}}^2 + 2m_e E_{\mathrm{binding}})^{1/2} .$$

This will enhance the interaction with the field and hence increase the ionization rate.

The modification of the Keldysh theory to quantitatively take into account the effect of the Coulomb field of the residual ion on the outgoing electron is the subject of some of our present work and will be discussed in a forthcoming publication.[16]

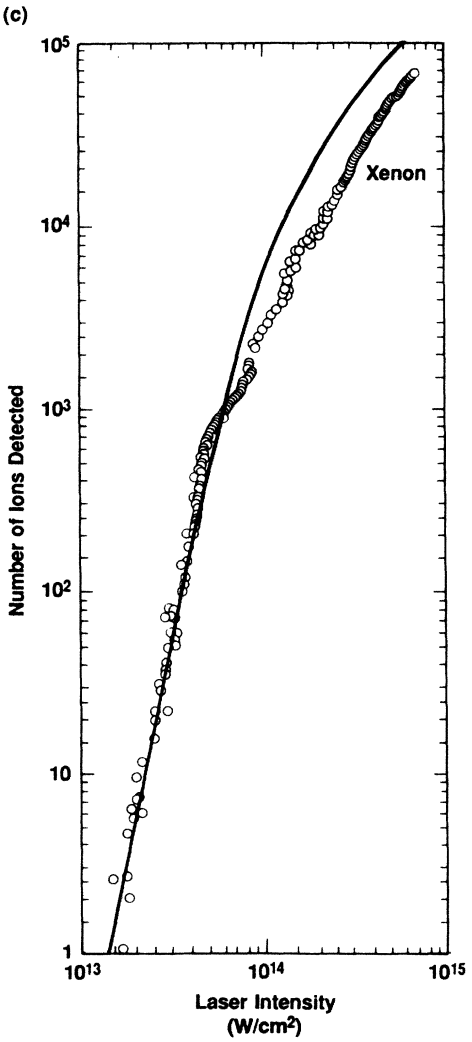

FIG. 8. (*Continued*).

III. CONCLUSION

We have examined the nonresonant multiphoton ionization of the rare gases Ar, Kr, and Xe at $\lambda=0.586\ \mu m$ as a function laser intensity in the range $10^{13} \leq I \leq 5\times 10^{14}$ W/cm^2 using a picosecond dye-laser system. The ion yield of up to Xe^{6+}, Kr^{4+}, and Ar^{3+} was determined by counting the actual numbers of ions detected with a time-of-flight mass spectrometer. This technique provides direct quantitative comparison of the empirically determined ion yields with that predicted by theory. For such comparison we developed a rate-equation kinetic model which can include ionization to multiply charged states via direct processes.

No evidence was found to suggest that the higher charge states are formed via a direct process from the ground state of the neutral atom. On the contrary, we obtained an adequate fit to the data using perturbation theory and assuming purely sequential ionization (i.e., Xe^{2+} is formed from Xe^{1+}, etc.). A general smooth increase in the threshold intensity for ionization with the number of photons absorbed is also observed. This was a general result, independent of the atomic species. This in turn suggests that the nonresonant ionization rate is a fairly weak function of the details of the atomic structure. In fact, the ionization rate appears to be dominated by the outgoing electron and gross features of the atom via the ionization potential.

The theory first presented by Keldysh in 1965 arrived at the same qualitative results as described above. Quantitative agreement between this theory and our experimental results is excellent for the formation of the singly charged ions but breaks down quickly when higher charge states are considered. The Keldysh theory should become even more applicable to the formation of singly charged ions under conditions where the tunneling parameter γ becomes less than unity. Our experiments covered a range $1.5 \leq \gamma \leq 4$. The general breakdown of the Keldysh theory for predicting the formation of higher charge states is probably due to the neglect of the effect of the Coulomb field of the residual ion on the outgoing electron wave function. A modification of this theory to explicitly account for the Coulomb field of the ion is presently being undertaken.

As a final note, we have explicitly avoided intermediate high-order resonances, both experimentally and theoretically in the work described herein. The behavior of these resonances in an intense field is of course an important question and is the subject of much of our present experimental effort.

ACKNOWLEDGMENTS

We would like to thank N. Hinsey for his technical assistance and also to acknowledge the Institutional Research and Development Program at the Lawrence Livermore National Laboratory for supporting this work. One of us (M.D.P.) would also like to acknowledge the support of the Nuclear Engineering, Health Physics and Radioactive Waste Management program administered by Oak Ridge Associated Universities for the U.S. Department of Energy. This work was performed under the auspices of the U.S. Department of Energy by the Lawrence Livermore National Laboratory under Contract No. W-7405-ENG-48.

[1]G. S. Voronov and N. B. Delone, Zh. Eksp. Teor. Fiz **50**, 78 (1966) [Sov. Phys.—JETP **23**, 54 (1966)].

[2]P. Agostini *et al.*, IEEE J. Quantum Electron. **QE-4**, 667 (1968); L. A. Lompre, G. Mainfray, C. Manus, and J. Thebault, Phys. Rev. A **15**, 1604 (1977).

[3]U. Johann, T. S. Luk, H. Egger, and C. K. Rhodes, Phys. Rev. A **34**, 1084 (1986).

[4]A. L'Hullier, L. A. Lompre, G. Mainfray, and C. Manus, Phys. Rev. A **27**, 2503 (1983).

[5]L. V. Keldysh, Zh. Eksp. Teor. Fiz. **47**, 1945 (1964) [Sov. Phys.—JETP **20**, 1307 (1965)].

[6]D. M. Volkov, Z. Phys. **94**, 250 (1935).

[7]O. L. Landen, M. D. Perry, and E. M. Campbell, Phys. Rev. Lett. **59**, 2558 (1987).

[8]E. P. Ippon and C. V. Shank, in *Ultrashort Light Pulses: Picosecond Techniques,* edited by S. L. Shapiro (Springer-Verlag, Berlin, 1978), p. 83.

[9]S. A. Fields *et al.*, Rev. Sci. Instrum. **48** (1977).

[10]M. R. Cervenan and N. R. Isenor, Opt. Commun. **13**, 175 (1975).

[11]T. W. B. Kibble, Phys. Rev. **150**, 1060 (1966).

[12]M. H. Mittleman, Phys. Rev. A **29**, 2245 (1984).

[13]P. Kruit, J. Kimman, H. G. Muller, and M. J. van der Wiel, Phys. Rev. A **28**, 248 (1983).

[14]P. H. Bucksbaum, R. R. Freeman, M. Bashkansky, and T. J. McIlrath, J. Opt. Soc. Am. B **4**, 760 (1987).

[15]A. L'Hullier, L. A. Lompre, G. Mainfray, and C. Manus, J. Phys. B **16**, 1363 (1983).

[16]M. D. Perry, A. Szöke, and O. L. Landen, Phys. Rev. Lett. (to be published).